JACS
JOURNAL OF THE AMERICAN CHEMICAL SOCIETY
Article
pubs.acs.org/JACS

Design and Evaluation of a Crystalline Hybrid of Molecular Conductors and Molecular Rotors

Cyprien Lemouchi,[†] Cécile Mézière,[†] Leokadiya Zorina,[†,‡] Sergey Simonov,[†,‡] Antonio Rodríguez-Fortea,[§] Enric Canadell,*[,∥] Pawel Wzietek,*[,⊥] Pascale Auban-Senzier,[⊥] Claude Pasquier,[⊥] Thierry Giamarchi,*[,#] Miguel A. Garcia-Garibay,*[,▽] and Patrick Batail*[,†]

[†]Laboratoire MOLTECH-Anjou, CNRS and Université d'Angers, UMR 6200, 49045 Angers, France

[‡]Institute of Solid State Physics RAS, 142432 Chernogolovka MD, Russia

[§]Departament de Química Física i Inorgànica, Universitat Rovira i Virgili, Marcel·lí Domingo s/n, 43007 Tarragona, Spain

[∥]Institut de Ciència de Materials de Barcelona (ICMAB-CSIC), Campus de la UAB, 08193 Bellaterra, Spain

[⊥]Laboratoire de Physique des Solides, CNRS and Université de Paris-Sud, UMR 8502, 91405 Orsay, France

[#]DPMC-MaNEP, University of Geneva, 24 Quai Ernest-Ansermet, CH-1211 Geneva, Switzerland

[▽]Department of Chemistry, University of California—Los Angeles, 607 Charles E. Young Drive East, Los Angeles, California 90095-1569, United States

Supporting Information

ABSTRACT: Combining recent concepts from the fields of molecular conductivity and molecular machinery we set out to design a crystalline molecular conductor that also possesses a molecular rotor. We report on the structures, electronic and physical properties, and dynamics of two solids with a common 1,4-bis(carboxyethynyl)bicyclo[2.2.2]octane (BABCO) functional rotor. One, $[n\mathrm{Bu_4N^+}]_2[\mathrm{BABCO}][\mathrm{BABCO^-}]_2$, is a colorless insulator where the dicarboxylic acid cocrystallizes with two of its monoanionic conjugated bases. The other is self-assembled by electrocrystallization in the form of black, shiny needles, with highly conducting molecular slabs of $(\mathrm{EDT\text{-}TTF\text{-}CONH_2})_2^+$ (EDT-TTF = ethylenedithiotetrathiafulvalene) and anionic [BABCO$^-$] rotors. Using variable-temperature (5−300 K) proton spin−lattice relaxation, $^1\mathrm{H}\ T_1^{-1}$, we were able to assign two types of Brownian rotators in $[n\mathrm{Bu_4N^+}]_2[\mathrm{BABCO}][\mathrm{BABCO^-}]_2$. We showed that neutral BABCO groups have a rotational frequency of 120 GHz at 300 K with a rotational barrier of 2.03 kcal mol^{-1}. Rotors on the BABCO$^-$ sites experience stochastic 32 GHz jumps at the same temperature over a rotational barrier of 2.72 kcal mol^{-1}. In contrast, the BABCO$^-$ rotors within the highly conducting crystals of $(\mathrm{EDT\text{-}TTF\text{-}CONH_2})_2^+[\mathrm{BABCO^-}]$ are essentially "braked" at room temperature. Notably, these crystals possess a conductivity of 5 S cm^{-1} at 1 bar, which increases rapidly with pressure up to 50 S cm^{-1} at 11.5 kbar. Two regimes with different activation energies E_a for the resistivity (180 K above 50 and 400 K below) are observed at ambient pressure; a metallic state is stabilized at ca. 8 kbar, and an insulating ground state remains below 50 K at all pressures. We discuss two likely channels by which the motion of the rotors might become slowed down in the highly conducting solid. One is defined as a low-velocity viscous regime inherent to a noncovalent, physical coupling induced by the cooperativity between five C_{sp3}−H···O hydrogen bonds engaging any rotor and five BABCO units in its environment. The rotational barrier calculated with the effect of this set of hydrogen bonds amounts to 7.3 kcal mol^{-1}. Another is quantum dissipation, a phenomenon addressing the difference of dynamics of the rotors in the two solids with different electrical properties, by which the large number of degrees of freedom of the low dimensional electron gas may serve as a bath for the dissipation of the energy of the rotor motion, the two systems being coupled by the Coulomb interaction between the charges of the rotors (local moments and induced dipoles) and the charges of the carriers.

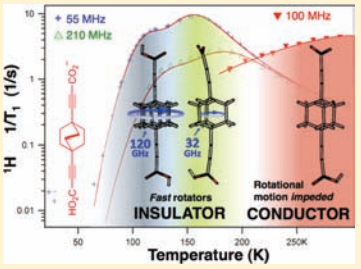

INTRODUCTION

We report on a materials discovery initiative designed to fashion a system whereby highly conducting molecular slabs and Brownian rotators are assembled, intertwined in the solid state. Our idea is to design conducting molecular systems with a rotator component where the dielectric modulation inherent to the rotor dynamics[1,2] may affect the electrostatic potential of the charge carriers' environment[3] and interfere with Mott transitions between conducting and localized states.[4] This would be especially relevant in those instances where nearest, next nearest neighbors, or longer range electrostatic interactions, rather than primarily electron correlations, become paramount in driving the localization.[5] A companion benefit would be to create situations where the rotor dynamics might couple with the magnetic dipoles of the $S = {}^1/_2$ carrier spins,[2]

Received: February 14, 2012
Published: April 13, 2012

   dx.doi.org/10.1021/ja301484b | J. Am. Chem. Soc. 2012, 134, 7880−7891

bringing in opportunities for unprecedented electronic and magnetic instabilities in otherwise rich phase diagrams where many competing ground states like charge and spin density waves, and antiferromagnetic and superconducting ground states, are being intensely investigated.[5−7] By designing conducting amphidynamic crystals with rapidly moving parts, we intend to bring together in the form of complex functional materials the fields of molecular machines[1,8] and amphidynamic solids[9] with the field of multifunctional conducting and magnetic molecular solids,[10] an approach complementary to recent work by Akutagawa, Nakamura, and co-workers.[2]

Molecular systems based on conjugated carboxylates have been developed in recent years to serve as functional components in the fields of organic conductors,[3,10] and organic electrodes for batteries.[11] We now report on 1,4-bis-(carboxyethynyl)bicyclo[2.2.2]octane (BABCO) (Scheme 1)

Scheme 1

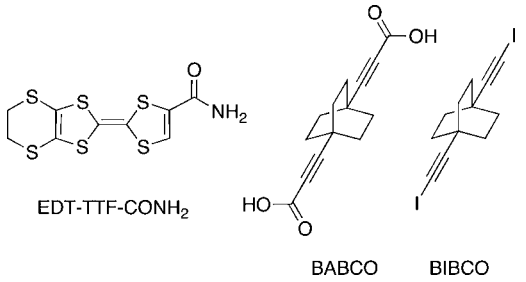

and the tetrabutylammonium salt of its monodeprotonated anion, $[n\mathrm{Bu_4N^+}]_2[\mathrm{BABCO}][\mathrm{BABCO^-}]_2$, to serve as rotator anionic components in the radical cation salt, $(\mathrm{EDT\text{-}TTF\text{-}CONH_2})_2{}^+[\mathrm{BABCO^-}]$ (EDT-TTF = ethylenedithiotetrathiafulvalene), where an electron localization at ambient pressure is suppressed at 8 kbar. The amide-functionalized ethylenedithiotetrathiafulvalene, EDT-TTF-$CONH_2$ (Scheme 1), was selected to be assembled with the $BABCO^-$ rotator to exploit the structure-directing ability of the redox-activated hydrogen bond donor character of the amide in molecular metals.[10e,12] The selection of bicyclo[2.2.2]octane as a rotator was based on its relatively high symmetry with a 3-fold rotational axis, which has been shown to display room temperature exchange dynamics in the gigahertz regime, even in relatively dense molecular solids.[9,13]

An unexpected outcome of the work reported herein was disclosed by variable temperature ^{1}H spin−lattice relaxation (T_1) experiments carried out at different fields on crystalline samples, confirming that static crystal NMR is emerging[2,13a] as a powerful approach to investigate the rotors dynamics in molecular machines. It is found that both the BABCO and $BABCO^-$ rotors in $[n\mathrm{Bu_4N^+}]_2[\mathrm{BABCO}][\mathrm{BABCO^-}]_2$ undergo fast, albeit different, stochastic movements, yet the molecular rotors are slowed down to a considerable extent in the low dimensional molecular conductor, $(\mathrm{EDT\text{-}TTF\text{-}CONH_2})_2{}^+[\mathrm{BABCO^-}]$. This prompted us to establish the important influence that C_{sp3}−H···O hydrogen bonds can have upon the modulation of the effective potential of molecular rotors. In addition, the possibility of quantum dissipation is introduced, a complementary phenomenon by which the classical or quantum movement of BABCO rotors might become "damped" by electronic quantum mechanical effects in the highly conducting solid.

EXPERIMENTAL SECTION

Synthesis of $HO_2C-BCO-CO_2H$ (BABCO) and $[nBu_4N^+]_2[BABCO][BABCO^-]_2$. Samples of 1,4-bis(carboxyethynyl)-bicyclo[2.2.2]octane (BABCO) were obtained in 81% yield as described in Scheme 2 from the terminal dialkyne 1,4-diethynylbicyclo[2.2.2]octane (BCO) synthesized from diethylsuccinate in a nine-step sequence reported earlier.[13a]

To a solution of 1,4-diethynylbicyclo[2,2,2]octane (200 mg, 1.26 mmol) in 50 mL of dried THF, cooled down to −78 °C, was added *n*-butyllithium (2.5 M in *n*-hexane) (1.2 mL, 3 mmol) under inert atmosphere and anhydrous conditions, and the mixture was stirred at −78 °C for 30 min. Note that our procedure uses *n*-butyllithium at variance with the synthesis of a series of phenylenedipropynoic acids reported earlier which uses EtMgBr instead.[14] Dried carbon dioxide was then bubbled through the solution while the reaction mixture was slowly warmed up to room temperature. The reaction was monitored by thin layer chromatography (ethylacetate/*n*-heptane =50:50). Then, the reaction mixture was acidified to a pH of 1 with a 6 M HCl aqueous solution, and it was extracted with dichloromethane. The organic layer was washed twice with cold water and then dried over magnesium sulfate, filtered, and evaporated to dryness under low pressure to afford a colorless oil that solidifies immediately at room temperature as a white solid (250 mg, 1.02 mmol, yield = 81%). Good quality plate-shaped single crystals of BABCO, whose structure is shown in Figure 1c, were obtained by slow evaporation of a solution of BABCO in a 50/50 (volume to volume) ethylacetate/*n*-heptane mixture. T_{decomp}: 201.7 °C. ^{1}H NMR (DMSO-d_6, 500 MHz): δ 1.76 (s, 12H). ^{13}C NMR (DMSO-d_6, 500 MHz): δ 154.30, 92.64, 74.27, 29.96, 25.80. ESI(+) m/z = 490.55 $[2(M - H)^-]$. Anal. Calcd for $C_{14}H_{14}O_4$: C, 68.28; H, 5.73. Found: C, 68.24; H, 6.17. Large, colorless cube-like single crystals of $[n\mathrm{Bu_4N^+}]_2[\mathrm{BABCO}][\mathrm{BABCO^-}]_2$ were found to crystallize out of the 11/1 CH_3CN/CH_3OH solvent mixture in the electrocrystallization cell.

Synthesis of $(\mathrm{EDT\text{-}TTF\text{-}CONH_2})_2{}^+[\mathrm{BABCO^-}]$. A two-compartment cell[15] equipped with platinum electrodes (l = 2 cm, Ø = 1 mm) and kept at 40 °C was filled with an acetonitrile (11 mL, dried over B alumina) solution and a 1 mL freshly distilled methanol solution containing 3-amido-3′,4′-ethylenedithiotetrathiafulvalene,[16] EDT-TTF-$CONH_2$ (5 mg) (Scheme 1), and $[n\mathrm{Bu_4N^+}]_2[\mathrm{BABCO}][\mathrm{BABCO^-}]_2$ (Scheme 2) (25 mg) which serves as electrolyte. Oxidation at low

Scheme 2

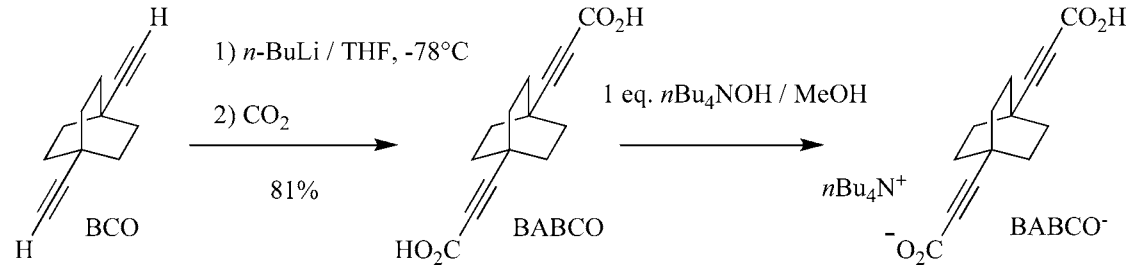

dx.doi.org/10.1021/ja301484b | J. Am. Chem. Soc. 2012, 134, 7880−7891

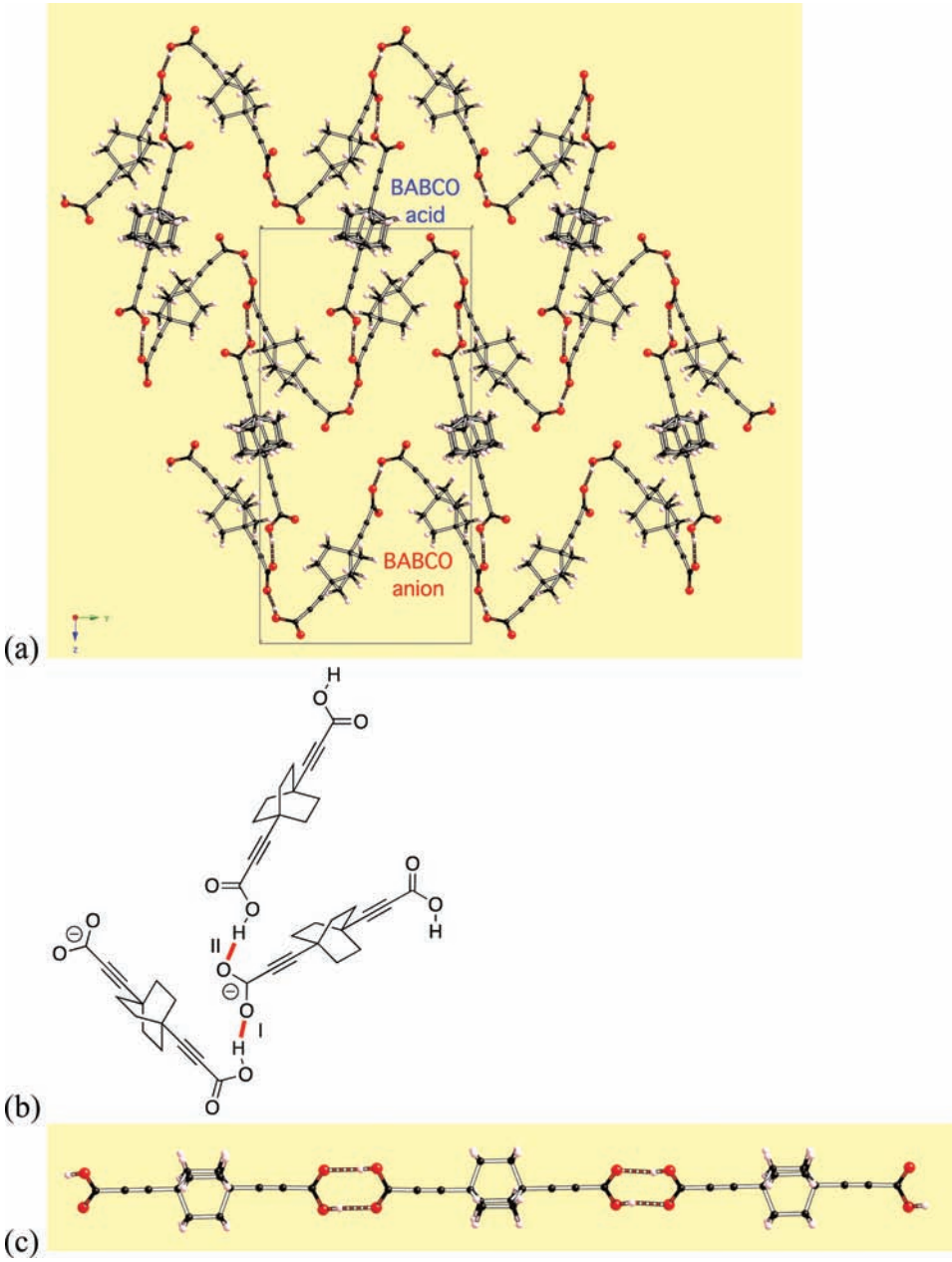

Figure 1. (a) Illustration of the two-dimensional hydrogen bonded net in $[n\mathrm{Bu_4N^+}]_2[\mathrm{BABCO}][\mathrm{BABCO^-}]_2$ (tetrabutylammonium cations are omitted for clarity). BABCO: C═O 1.207(2) Å, and C—O 1.318(2) Å. $\mathrm{BABCO^-}$: C═O 1.215(2) Å. C—O 1.305(2) Å, carboxylate C—O 1.243(2) Å and 1.268(2) Å. The BABCO rotors (neutral acid) are disordered over two positions while $\mathrm{BABCO^-}$ rotors are fully ordered. (b) The acid−base interface develops out of two robust O—H···O hydrogen bonds, I 1.69 Å and II 1.79 Å. (c) A hexagonal closed-packed array of infinite hydrogen bonded one-dimensional polymers, of which a fragment is shown here, constitutes the structure of the monomolecular neutral solid 1,4-bis(carboxyethynyl)bicyclo[2.2.2]octane (BABCO). Hydrogen-bonded carboxylic dimers[12c] are built out of two O−H···O hydrogen bonds; the four contacts in two independent strings are in the range 1.83−1.86 Å. Interestingly, this carboxylic dimer motif cannot be sustained in $[n\mathrm{Bu_4N^+}]_2[\mathrm{BABCO}][\mathrm{BABCO^-}]_2$ where the carboxylate oxygen atoms act as stronger hydrogen bond acceptors with shorter O—H···O hydrogen bonds, hence the single bonded motifs shown in part b.

constant current (0.2 μA) affords shiny, black plate-like single crystals after 10 days.

X-ray Structure Analysis. Crystal data for BABCO, $[n\mathrm{Bu_4N^+}]_2[\mathrm{BABCO}][\mathrm{BABCO^-}]_2$, and $(\mathrm{EDT\text{-}TTF\text{-}CONH_2})_2{}^+[\mathrm{BABCO^-}]$ are listed in Table 1. X-ray data were collected at room temperature for BABCO and $[n\mathrm{Bu_4N^+}]_2[\mathrm{BABCO}][\mathrm{BABCO^-}]_2$ and at 200 K for $(\mathrm{EDT\text{-}TTF\text{-}CONH_2})_2{}^+[\mathrm{BABCO^-}]$ using a Bruker Nonius KappaCCD diffractometer with monochromatized Mo Kα-radiation (λ = 0.710 73 Å, graphite monochromator, combined φ/ω-scan). All crystals of BABCO and $(\mathrm{EDT\text{-}TTF\text{-}CONH_2})_2{}^+[\mathrm{BABCO^-}]$ appeared to be nonmerohedral twins. Diffraction data from both twin domains were combined into a SHELX HKLF5 file and used for refinement of the structure BABCO; absorption correction of experimental intensities was made by an analytical method. The refined twin fraction for BABCO is 0.3077(7). Empirical absorption correction was applied for $[n\mathrm{Bu_4N^+}]_2[\mathrm{BABCO}][\mathrm{BABCO^-}]_2$ and $(\mathrm{EDT\text{-}TTF\text{-}CONH_2})_2{}^+[\mathrm{BABCO^-}]$ using the SADABS program.[17] The structures were solved by a direct method followed by Fourier syntheses and refined by a full-matrix least-squares method in an anisotropic approximation for all non-hydrogen atoms using the SHELX-97 programs.[18] H-atoms were placed in idealized positions

Table 1. Crystal Data, Data Collection, and Refinement Details

	BABCO	$[n\mathrm{Bu_4N^+}]_2[\mathrm{BABCO}][\mathrm{BABCO^-}]_2$	$(\mathrm{EDT\text{-}TTF\text{-}CONH_2})_2^+[\mathrm{BABCO^-}]$
λ/Å	0.710 73	0.710 73	0.710 73
T/K	293(2)	295(2)	200(1)
chemical formula	$C_{14}H_{14}O_4$	$C_{74}H_{112}N_2O_{12}$	$C_{32}H_{27}N_2O_6S_{12}$
mol wt	246.25	1221.66	920.28
cryst syst	monoclinic	monoclinic	monoclinic
a/Å	6.8168(13)	9.4781(3)	14.690(4)
b/Å	16.553(4)	13.8557(4)	6.6624(12)
c/Å	23.215(4)	27.3763(5)	18.941(11)
β/deg	101.414(17)	95.713(5)	96.85(3)
V/Å^3	2567.6(9)	3577.4(2)	1841(1)
space group, Z	$P2_1/c$, 8	$P2_1/c$, 2	Pa, 2
$F(000)$	1040	1332	946
$\rho_{calcd.}$/ g cm^{-3}	1.274	1.134	1.661
μ/cm^{-1}	0.93	0.75	7.61
T_{min}, T_{max}	0.9690, 0.9961	0.7010, 0.7456	0.6380, 0.7452
$2\theta_{max}$/deg	50.6	54.2	50.0
reflns collected	34313	58216	35569
indep reflns	34 313	7809	6350
R_{int}		0.0930	0.1198
no. of params	326	424	472
GOF on F^2	1.135	1.000	1.015
R1 [$I > 2\sigma(I)$]	0.1189	0.0565	0.0761
wR2 [$I > 2\sigma(I)$]	0.2084	0.1076	0.1787

and refined using a riding model with U_{iso}(H) fixed at 1.2U_{eq}(C, N) and 1.5U_{eq}(O).

VT ^{1}H Spin–Lattice Relaxation Time (T_1). Experiments were carried out at Orsay on static crystalline samples at two different ^{1}H Larmor frequencies (55 and 210 MHz) and over a wide range of temperatures (5–300 K). Wide-line ^{1}H spectra were measured in single crystals with a superconducting magnet using a NMR spectrometer and probe built at Orsay. The probe is designed so as to reduce spurious proton signals. Samples were loaded into a small glass tube (typically 1.2–1.6 mm in diameter, depending on the amount of material available) on which the NMR coil was wound. ^{1}H signals were recorded using the FID following a $\pi/2$ pulse (typically 0.8–1.5 μs), and spin–lattice relaxation was measured using the standard saturation recovery sequence. For each T_1 measurement we recorded signals for 20 values of the relaxation delay between the saturating comb and the measuring pulse.

Transport Measurements. In order to improve the quality of the contacts, gold pads were evaporated on the surface of single crystals of $(\mathrm{EDT\text{-}TTF\text{-}CONH_2})^+_2[\mathrm{BABCO^-}]$ before attaching gold wires with silver paste. A standard four points technique was used with low frequency ac current (I_{ac}= 1 μA) and lock-in detection. Resistivity measurements were also performed under hydrostatic pressure in a CuBe clamped cell up to 12 kbar with silicon oil (Daphne 7373) as pressure transmitting medium. The pressure at room temperature was extracted from the resistance of a manganin gauge located inside the pressure cell. The loss of pressure during cooling is estimated to 2 kbar, and the pressure indicated in Figure 6b is the low temperature value (P_{LT}). Resistivity measurements were performed in a cryocooler down to 20 K. A copper-constantan thermocouple inside the pressure cell was used as the thermometer.

Computational Details. The tight-binding band structure calculations[19] were of the extended Hückel type. A modified Wolfsberg–Helmholtz formula was used to calculate the nondiagonal H_{ij} values.[20] All valence electrons were taken into account in the calculations, and the basis set consisted of Slater-type orbitals of double-ζ quality for C, N, and O 2s and 2p, S 3s and 3p, and of single-ζ quality for H 1s. The ionization potentials, contraction coefficients, and exponents were taken from previous work.[21] The density functional theory (DFT) molecular calculations were carried out adopting the hybrid (GGA) B3LYP[22] and (meta-GGA) M06-2X[23] functionals using the Gaussian 09 code.[24] Basis sets of the type 6-311-G(d,p) were used.[25]

RESULTS AND DISCUSSION

$[n\mathrm{Bu_4N^+}]_2[\mathrm{BABCO}][\mathrm{BABCO^-}]_2$ Has Two Rotors with Different Environments and Rotational Potentials, One of Which, the BABCO Rotor, Is Faster. The crystal structure of large colorless blocks, with one-half independent BABCO and one independent $\mathrm{BABCO^-}$ in the asymmetric unit of the monoclinic unit cell, reveals the presence of a two-dimensional framework where hydrogen bonded neutral acid molecules pull apart hydrogen bonded strings of their monodeprotonated conjugated bases (Figure 1a). The pattern created out of two robust O–H···O hydrogen bonds at the acid–base interface is shown in Figure 1b. Interaction I, which holds together the $[\mathrm{BABCO^-}]_\infty$ polymer, has a characteristic, antiperiplanar configuration of the single O—H bond allowing it to reach out toward one carboxylate oxygen atom (Figure 1b). It is also far shorter than interaction II, the O—H···O hydrogen bond between BABCO and $\mathrm{BABCO^-}$. Note that the inventory of C=O and C—O bond lengths (Figure 1) leaves no ambiguity as far as identifying the molecules and the 2:1:2 net stoichiometry of this diluted salt. This makes for a softer lattice where the Madelung energy of the salt is reduced. A similar, yet charge inverted, situation has been observed for $(\mathrm{Hmel^+})(\mathrm{mel})[\mathrm{Au(midt)_2^-}]\cdot 2\mathrm{DMF}\cdot 2\mathrm{H_2O}$ where mel stands for melamine and midt for maleimide dithiolato.[26]

Variable temperature spin–lattice relaxation data, ^{1}H T_1^{-1}, are being intensively scrutinized since they are particularly useful when the stimulated nuclear transitions responsible for restoring thermal equilibrium in the sample are determined by the modulation of dipolar interactions caused by the rapid motion of internal rotors.[2,9,13a] Note that the dynamics of the rotors in BABCO and $\mathrm{BABCO^-}$ in crystals of $[n\mathrm{Bu_4N^+}]_2[\mathrm{BABCO}][\mathrm{BABCO^-}]_2$ is likely to differ because there is only one equilibrium position for the $\mathrm{BABCO^-}$ rotor in contrast to a disorder over two equilibrium positions on the neutral BABCO rotor site (Figure 1a). Thus, as demonstrated previously for 1,4-bis(iodoethynyl)bicyclo[2.2.2]octane (BIBCO, Scheme 1),[13a] ordered and disordered sites have potentials with 3-fold and 6-fold rotational axes that correspond, respectively, to high and low energy barriers. Therefore, the barrier for the disordered BABCO rotors on the higher symmetry site is expected to be lower than that for the ordered $\mathrm{BABCO^-}$ rotors. This prompted us to conduct variable temperature ^{1}H T_1^{-1} experiments on static crystals at two fields, 55 and 210 MHz (Figure 2), to probe dynamic processes occurring at frequencies that are near the Larmor frequency of the ^{1}H nucleus.

The data in Figure 2 reveals two T_1^{-1} maxima shifted to higher temperatures for larger magnetic fields, as expected. Note that the magnitudes of T_1^{-1} for each of these maxima are not identical. Instead, the maximum at lower temperature is smaller, an indication that fewer mobile protons contribute to

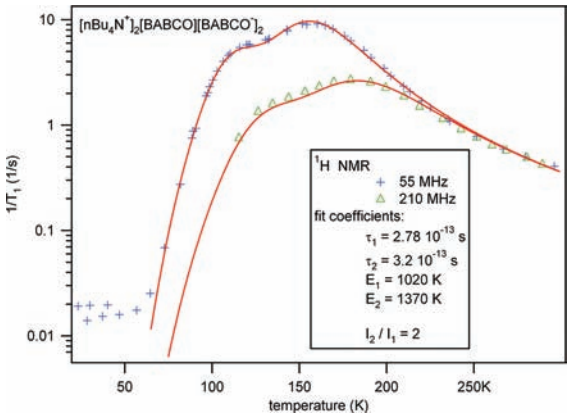

Figure 2. Variable temperature ^{1}H spin–lattice relaxation time at 55 and 210 MHz for $[n\mathrm{Bu_4N^+}]_2[\mathrm{BABCO}][\mathrm{BABCO^-}]_2$. Note the excellent, robust fits (red solid lines) of the data to the Kubo–Tomita equation, assuming an Arrhenius behavior for the temperature dependence of rotational correlation time, $\tau_c = \tau_0 \exp(E_a/kT)$, for a 2:1 proportion of the number of mobile C–H on the $\mathrm{BABCO^-}$ and BABCO sites, respectively.

this relaxation process. Since there are twice as many $\mathrm{BABCO^-}$ rotors on the ordered sites in $[n\mathrm{Bu_4N^+}]_2[\mathrm{BABCO}][\mathrm{BABCO^-}]_2$ than BABCO rotors on the disordered sites, robust, excellent fits of the T_1^{-1} data (Figure 2 and Table 2) to the Kubo–Tomita model of two thermally activated Arrhenius processes for the ^{1}H spin–lattice relaxation of mobile protons in a 1:2 ratio on two sites with a common spin temperature allow us to unambiguously assign to the BABCO rotors the rotational barrier with the lower energy. Note in addition that the excellent fits of the two T_1^{-1} maxima neatly exacted for a 12:24 proportion of mobile protons demonstrate that the only motion contributing to the relaxation is that of the rotors.

This analysis of the data is conducted under the reasonable assumption that the motion of the two rotors located on two different sites is not correlated. Note however that our measurements should not be very sensitive to any kind of such correlation because the rotors are far enough on those two sites so that the inter-rotor spin–spin couplings are negligible, thereby justifying a fit as the sum of two independent processes.

Arrhenius parameters derived from Kubo–Tomita fits of the T_1 data for both thermally activated relaxation processes with a common spin temperature in $[n\mathrm{Bu_4N^+}]_2[\mathrm{BABCO}][\mathrm{BABCO^-}]_2$ and BIBCO[13] are compared in Table 2.[27] In both solids, the rotators on the less constrained sites, that is, those sites with two disordered positions, have the lower rotational barrier. Interestingly, the attempt frequency (or pre-exponential factor A) for the disordered BABCO rotors is larger than that for the ordered $\mathrm{BABCO^-}$ rotors, when the reverse is observed for the two sites in crystals of BIBCO. The attempt frequency represents the highest jumping frequency for the thermally activated rotor and differs significantly for the rotators in different environments in $[n\mathrm{Bu_4N^+}]_2[\mathrm{BABCO}][\mathrm{BABCO^-}]_2$ and in BIBCO as well. It is related to the frequency of the librational modes of oscillation of the rotator and is determined by the shape of the potential,[13a] a valuable characteristic of the environment of the rotors in the solid state. The development of a library of data, obtained by extending Table 2 to include a large set of crystalline systems, will be invaluable to allow for a compared, comprehensive analysis of the similarity and differences of the crystal chemistry features of the environments of such rotors with similar or different attempt frequencies and rotational barriers for their thermally activated movements in the solid state. Finally, the calculated rates of room temperature rotation (Table 2) yield values of 120 and 32 GHz for BABCO and $\mathrm{BABCO^-}$ rotators, respectively, which signal that these fast rotors are somewhat slower than both rotors in the disordered and ordered layers in BIBCO.

$(\mathrm{EDT\text{-}TTF\text{-}CONH_2})^+_2[\mathrm{BABCO^-}]$: A δ-Type Layer Topology and a Very Slow Rotor. As shown in Figure 3, slabs of

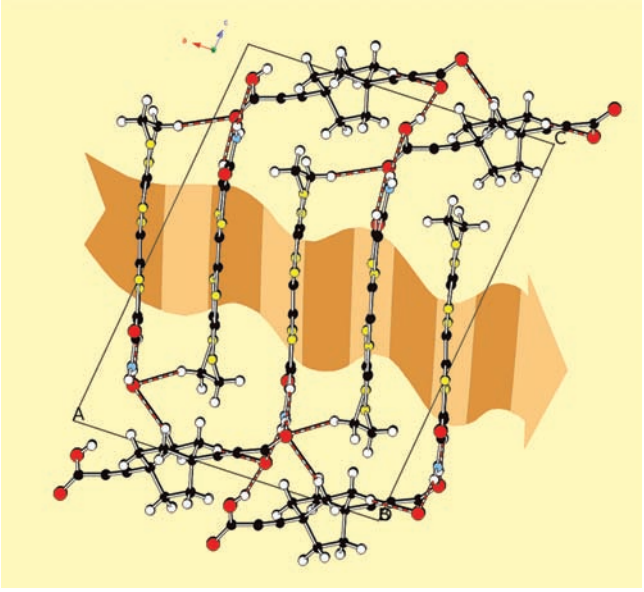

Figure 3. Structure of $(\mathrm{EDT\text{-}TTF\text{-}CONH_2})_2^+[\mathrm{BABCO^-}]$. One equilibrium position only is identified for the $\mathrm{BABCO^-}$ rotors. The undulating arrow encompasses the overlapping radical cations and symbolizes the conducting slab, also shown in Figure 7.

organic radical cations alternate along c with $\mathrm{BABCO^-}$ layers. The donor layer topology is analyzed in relation to its electronic structure in the following section. There are two $\mathrm{EDT\text{-}TTF\text{-}CONH_2}$ and one $\mathrm{BABCO^-}$ molecules in the

Table 2. Arrhenius Parameters Derived from Fits (Figure 2) of the T_1^{-1} Data to the Kubo–Tomita Equation, $\tau_c = \tau_0 \exp(E_a/kT)$, for BIBCO and $[n\mathrm{Bu_4N^+}]_2[\mathrm{BABCO}][\mathrm{BABCO^-}]_2$

	BIBCO[13]		$[n\mathrm{Bu_4N^+}]_2[\mathrm{BABCO}][\mathrm{BABCO^-}]_2$	
	disordered layer	ordered layer	disordered BABCO site	ordered $\mathrm{BABCO^-}$ site
E_a (kcal mol^{-1})	1.48	2.75	2.03	2.72
E_a (K)	745	1384	1020	1370
A (s^{-1})	5.21×10^{12}	8.00×10^{12}	3.6×10^{12}	3.1×10^{12}
τ_0 (s)	1.92×10^{-13}	1.25×10^{-13}	2.78×10^{-13}	3.2×10^{-13}
frequency at 300 K (GHz)	430[13b]	77[13b]	120	32

dx.doi.org/10.1021/ja301484b | J. Am. Chem. Soc. 2012, 134, 7880–7891

asymmetric unit. A set of hydrogen bond donor and acceptor functionalities, described in Figure 4, competes in the self-assembly process at the platinum electrode during crystal growth. The inventory includes the N–H, C_{sp2}–H, and C_{sp3}–H hydrogen bond donors of EDT-TTF-$CONH_2$,[12,16] the O–H hydrogen bond donor of the carboxylic acid group, the C_{sp3}–H hydrogen bond donors of the three ethylene bicyclo[2.2.2]-octane rotor blades, and the C=O hydrogen bond acceptors of the carboxylic acid and primary amide although the strength of the latter is expected to be weakened in radical cation forms.[12a] In addition, because of the outer ethylene groups and the bicyclo[2.2.2]octane rotators, there is the potential for subtle, yet attractive,[28] C_{sp3}–H···H–C_{sp3} dihydrogen homo- or heterodispersive van der Waals contacts to involve these linear or polyhedral alkanes.

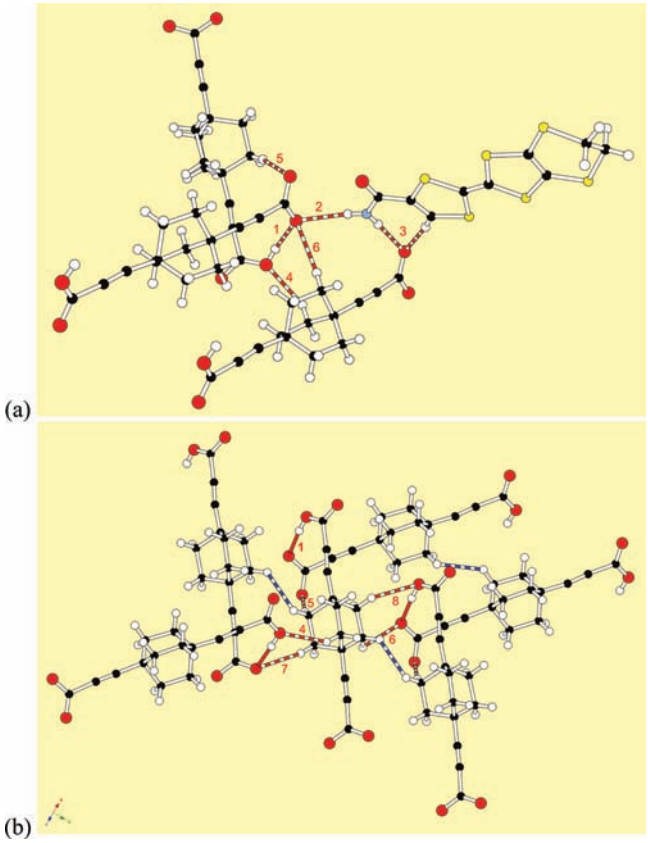

Figure 4. Illustration of the hydrogen bond interactions **1**–**8** in (EDT-TTF-$CONH_2$)$_2^+$[$BABCO^-$]. The values for H···O separations are (a) **1** O–H···O, 1.72 Å; **2** N–H···O, 2.34 Å; **3** N–H···O, 2.21 Å; and C_{sp2}–H···O, 2.26 Å. (b) Note also the set of five C_{sp3}–H···O hydrogen bonds involving the ethylene rotor blades: **4** 2.46 Å; **5** 2.66 Å; **6** 2.72 Å; as well as **7** 2.71 Å and **8** 2.74 Å. In addition, one dihydrogen contact, H···H: 2.40 Å,[28] is identified by a dotted blue line.

Two salient features stand out in Figure 4. First, the strongest hydrogen bond is **1**, the O–H···O interaction between $BABCO^-$ anions, and its topology, again with a characteristic antiperiplanar O–H configuration (Figure 4), is nearly identical, albeit not as strong (**1**: 1.72 Å in Figure 4), to that (**I**: 1.69 Å in Figure 1b) which makes for strings of $BABCO^-$ molecules in [$n$$Bu_4N^+$]$_2$[BABCO][$BABCO^-$]$_2$. Therefore, it is of interest to note that the structure of (EDT-TTF-$CONH_2$)$_2^+$[$BABCO^-$] shown in Figure 3 relates to that of [$n$$Bu_4N^+$]$_2$[BABCO][$BABCO^-$]$_2$ in Figure 1a simply by substituting the radical cation slab for the neutral acid molecules, keeping with hydrogen bonded [$BABCO^-$]$_\infty$ strings. The flexible, zigzag arrangement of $BABCO^-$ units in a string easily adapts to the crystal environment. For example, the angle between long molecular axes within the string increases from 56° in [$n$$Bu_4N^+$]$_2$[BABCO][$BABCO^-$]$_2$ to 98° in (EDT-TTF-$CONH_2$)$_2^+$[$BABCO^-$] (see Figures 1a and 4 for a comparison). Within a string the topology of O–H···O bonds also changes from antiperiplanar–synperiplanar to antiperiplanar–antiperiplanar, respectively. Second, five intermolecular contacts with participation of H-atoms from the three bicyclo[2.2.2]octane ethylene rotor blades are identified in Figure 4; they include C_{sp3}–H···O hydrogen bonds with –COOH and $-COO^-$ groups of neighboring $BABCO^-$ (H···O 2.46, 2.66, 2.71, 2.72, and 2.74 Å, C_{sp3}–H···O angles: 140°, 169°, 168°, 168°, and 136°, respectively). Furthermore, one short C_{sp3}–H···H–C_{sp3} dihydrogen contact is identified between rotor blades of neighboring bicyclo[2.2.2]octane rotators (Figure 4b). Note that with a H···H intermolecular contact distance at 2.40 Å, this interaction is comparable to *intramolecular* H···H contacts in the ordered BCO rotor. This contact distance appears to be similar to the shorter attracting contacts between alkanes, like 2.406 Å in dodecahedrane, which have been shown to store as much as 2.87 kcal mol^{-1}.[28]

The variable temperature ^{1}H T_1 data at 100 MHz for (EDT-TTF-$CONH_2$)$_2^+$[$BABCO^-$] are shown in Figure 5. In stark contrast with the data in Figure 2, the ^{1}H spin–lattice relaxation is much slower than for [$n$$Bu_4N^+$]$_2$[BABCO]-[$BABCO^-$]$_2$. The small increase in T_1^{-1} between 180 and 280 K (the relaxation time is far too long to warrant investigations at lower temperatures) demonstrates that if there is a maximum it will appear well above room temperature. Hence, the data in Figure 5 demonstrate that the $BABCO^-$ rotors are comparatively braked in within the solid in (EDT-TTF-$CONH_2$)$_2^+$[$BABCO^-$], a remarkable outcome when both the BABCO and $BABCO^-$ rotors undergo very fast stochastic movements in [$n$$Bu_4N^+$]$_2$[BABCO][$BABCO^-$]$_2$.

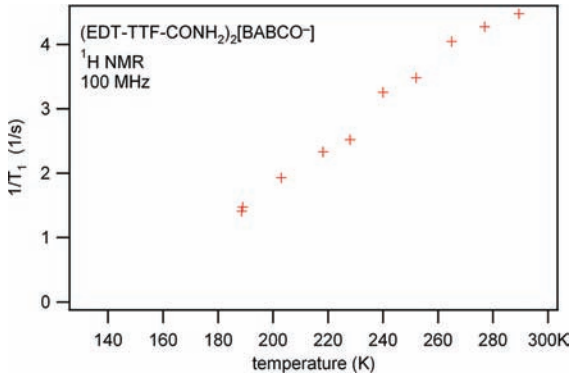

Figure 5. Variable temperature ^{1}H reciprocal spin–lattice relaxation time T_1^{-1} at 100 MHz for (EDT-TTF-$CONH_2$)$_2^+$[$BABCO^-$].

In the wake of the recent study of the analogous BIBCO,[13] these results demonstrate how valuable static crystal NMR investigations of variable temperature ^{1}H spin–lattice relaxation are to characterize and analyze the rotor dynamics in molecular machines. Key defining parameters like activation energy, attempt frequency, and frequency of rotation at 300 K (Table 2) need to be determined and sorted out for frictionless rotators in a large set of different solid state environments. This

dx.doi.org/10.1021/ja301484b | J. Am. Chem. Soc. 2012, 134, 7880–7891

would help to unravel what, in a gallimaufry of competing intermolecular interactions defining a rotor environment, are the relevant criteria to identify those which are likely to affect their rotor rotational barrier.

Change of Conductivity Regime of (EDT-TTF-CONH$_2$)$^+_2$[BABCO$^-$] under Pressure. The room temperature conductivity, σ, is 5 S cm^{-1} at 1 bar and increases rapidly with pressure up to 50 S cm^{-1} at 11.5 kbar. Despite high conductivity values, the temperature dependence of the resistivity, ρ, at P = 1 bar exhibits a localized behavior, $\rho = \rho_0 \exp(E_a/T)$. The log scale plot of the resistivity as a function of the inverse temperature (Figure 6a) presents two regimes

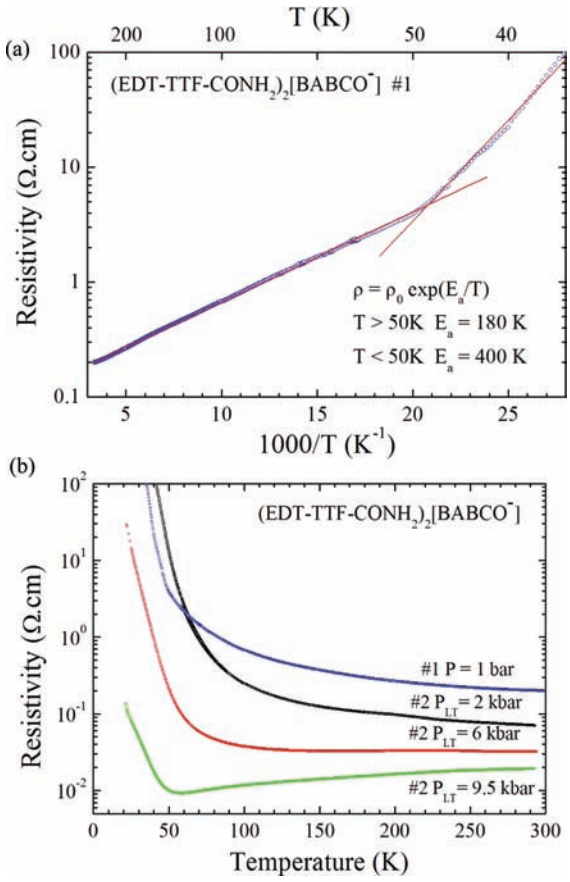

Figure 6. (a) Ambient pressure resistivity for (EDT-TTF-CONH$_2$)$_2^+$[BABCO$^-$] as a function of inverse temperature showing two different activation energies, E_a, below and above 50 K. The solid lines are a fit to the data. (b) Temperature dependence of the resistivity measured at several pressures on a second sample. The ambient pressure data shown in part a are also plotted (solid blue line) in part b.

with different activation energies E_a for the resistivity. Between room temperature and 50 K, E_a = 180 K is of the order of magnitude of the thermal energy while a larger value below 50 K, E_a = 400 K, suggests a phase transition at 50 K. The high temperature localization is progressively suppressed under pressure, and a metallic state is stabilized at about 8 kbar (Figure 6b). Note however that the insulating ground state remains well established below 50 K at all investigated pressures.

Electronic Structure of the Donor Layers. The donor layers of (EDT-TTF-CONH$_2$)$_2^+$[BABCO$^-$] are of the δ-type with four molecules in the repeat unit. As shown in Figure 7,

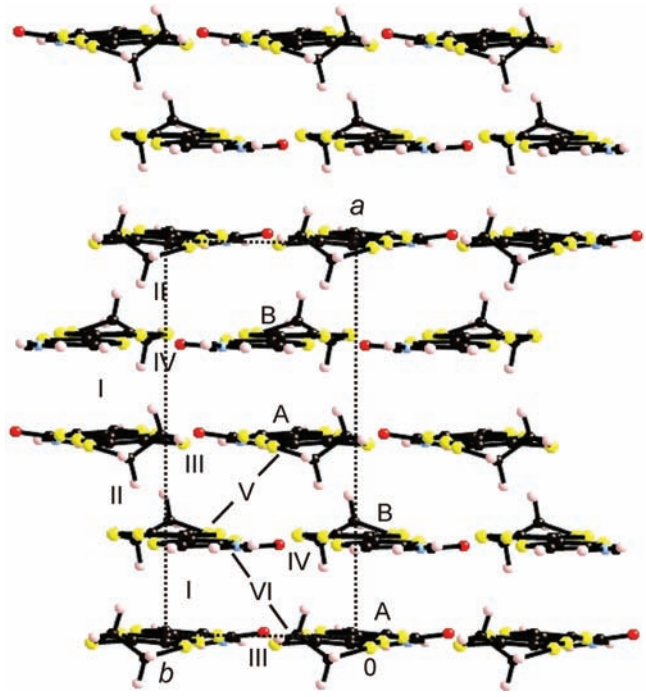

Figure 7. Donor layer of (EDT-TTF-CONH$_2$)$_2^+$[BABCO$^-$] where the six different types of donor···donor interactions are labeled.

here are two different donor molecules (noted A and B) and six different types of intermolecular interactions (noted I–VI). Donor A exhibits a central C=C bond length of 1.40(2) Å whereas donor B exhibits a considerably shorter one of 1.33(2) Å. As expected, the HOMO energies of the two donors are different (ΔE = 0.107 eV, the HOMO of B being lower) although not as much as one could expect on the basis of these C=C bond lengths. These bond lengths suggest that the two donors could be found as a cation and a neutral molecule.

In order to learn what is the appropriate description of these layers as far as the HOMO···HOMO interactions are concerned, i.e., those interactions responsible for the transport properties, we have calculated the $\beta_{HOMO-HOMO}$ interaction energies which are a sensitive measure of the strength of these interactions.[29] The calculated $|\beta_{HOMO-HOMO}|$ values for every type of HOMO···HOMO interaction as well as the associated S···S distances shorter than 4.0 Å are given in Table 3. On the basis of these HOMO···HOMO interaction energies it is clear that the donor lattice can be described as being built from interacting dimeric (A–B) units (interaction I). These dimers interact along *a* through interactions II and V, and along *b* through interactions III, IV, and VI. Bearing in mind that

Table 3. Calculated Values of the $|\beta_{HOMO-HOMO}|$ [eV] and S···S Distances Shorter Than 4.0 Å for the Different Donor···Donor Interactions in δ-(EDT-TTF-CONH$_2$)$_2^+$[BABCO$^-$]

interaction	S···S (Å)	$\lvert\beta_{HOMO-HOMO}\rvert$ (eV)
I (A···B)	3.569, 3.617, 3.670, 3.812, 3.870	0.4391
II (A···B)	3.834, 3.922	0.1742
III (A···A)	3.386, 3.484, 3,780, 3.905	0.1351
IV (B···B)	3.367, 3.539, 3.768, 3.859	0.1495
V (A···B)	3.750, 3.781, 3.868	0.2212
VI (A···B)		0.0681

dx.doi.org/10.1021/ja301484b | J. Am. Chem. Soc. 2012, 134, 7880–7891

because of the dimerization we must take the two combinations of the HOMOs, $\Psi_{\pm} \approx 1/\sqrt{2}(HOMO_A \pm HOMO_B)$, as the basis set to construct the band structure together with the values of Table 3, we must conclude that the HOMOs interact in a quite isotropic way within the layer plane. Since the repeat unit contains two equivalent dimers, the band structure will contain two well separated pairs of bands, the lower based on the bonding Ψ_- dimer orbital and the upper based on the antibonding Ψ_+ dimer orbital. Both pairs of bands should be two-dimensional in character.

The previous analysis is confirmed by the calculated band structure of Figure 8. Since the stoichiometry dictates that there must be two holes in these HOMO bands, the upper pair of bands must be half-filled. Because of the degeneracy along the X → M line, a consequence of the existence of a glide plane for the donor layer relating the two equivalent dimers along the *a* direction, and the fact that the dispersion of the partially filled bands is quite sizable (∼ 0.5 eV), one is led to the prediction that the salt could exhibit metallic behavior. The calculated Fermi surface assuming a metallic filling of the bands is shown in Figure 9. This Fermi surface can be described as the superposition of a series of closed pseudocircles with an area equal to 100% of the cross-section of the Brillouin zone. If the metallic state could be stabilized a magnetoresistance study would lead to the observation of two different Shubnikov–de Haas frequencies (∼ 25% and 100% of the cross sections of the Brillouin zone) and probably to additional frequencies due to quantum interference effects.

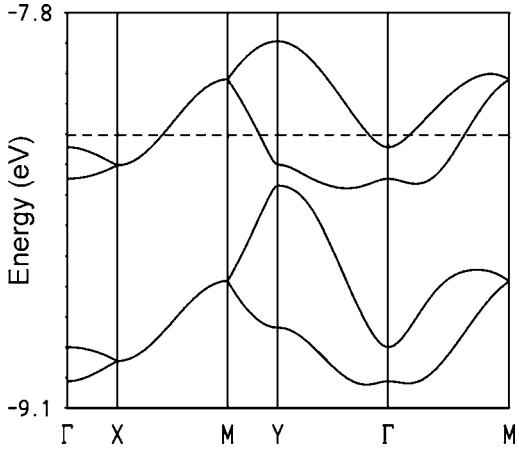

Figure 8. Calculated band structure for the donor layers of (EDT-TTF-$CONH_2)_2^+[BABCO^-]$, where the dashed line refers to the Fermi level assuming a metallic filling of the bands and Γ = (0, 0), X = (*a**/2, 0), Y = (0, *b**/2), and M = (*a**/2, *b**/2).

At this point, it is worth noting that the analysis of the transport properties of this salt based solely on the structural information would suggest an insulating behavior due to the charge localization as A^+ cations and B^0 neutral molecules. However, the electronic structure study leads to a very different conclusion (see for instance the density of states projections of Figure 10 which shows that the HOMOs of A and B mix strongly *in the whole energy range* of the HOMO bands providing support for our analysis in terms of dimer orbitals) which agrees with the high conductivity of the system. It should also be remarked that this salt differs from other salts with such twisted overlap within the dimer, like *β*-$(BEDT\text{-}TTF)_2AsF_6$ and related salts[30] which are generally more one-dimensional and thus exhibit good nesting properties leading to a metal to insulator transition.[31] The present salt is an almost ideal 2D system so that the metallic system should be very stable.

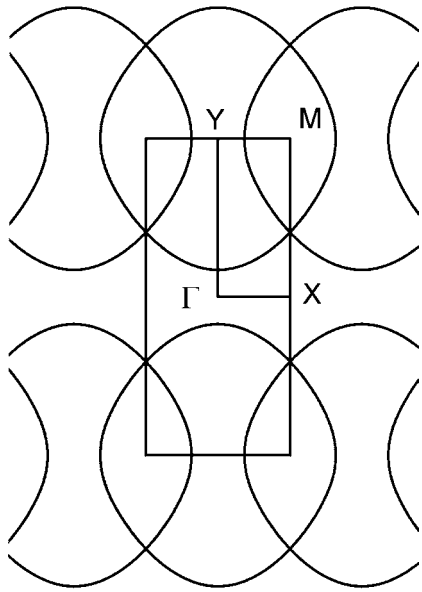

Figure 9. Calculated Fermi surface for the donor layers of (EDT-TTF-$CONH_2)_2^+[BABCO^-]$ assuming a metallic filling of the bands.

The essential result of the electronic structure study is that a metallic state is not only likely but compatible with the existence of two different donors with considerably different central C═C bond lengths. In other words, with the present structure both a localized state with charge disproportionation (i.e., a so-called charge ordered state[4]) and a delocalized, stable bidimensional metallic state are compatible ground states without practically any structural change. With this observation in mind our finding of a change from activated to nonactivated conductivity under pressure for (EDT-TTF-$CONH_2)^+{}_2[BABCO^-]$ can be easily understood.

Low-Velocity Viscous Regime Inherent to C_{sp3}–H···O Hydrogen Bond Interactions. Pondering about why *fast* rotors inside $[n Bu_4N^+]_2[BABCO][BABCO^-]_2$ are damped in $(EDT\text{-}TTF\text{-}CONH_2)_2^+[BABCO^-]$, one goes back to the former compared analysis of their crystal structures and note that the five C_{sp3}–H···O contacts (interactions 4–8 in Figure 4b), absent in $[n Bu_4N^+]_2[BABCO][BABCO^-]_2$, rather than perhaps a weak dihydrogen contact, are significant in defining the constraints, akin to a noncovalent, physical coupling at thermodynamic equilibrium between a rotator and five other BABCO units in its environment in (EDT-TTF-$CONH_2)^+{}_2[BABCO^-]$.

To see the effect of these intermolecular interactions on the rotational barrier of $BABCO^-$ in (EDT-TTF-$CONH_2)^+{}_2[BABCO^-]$, we carried out DFT calculations for an isolated $BABCO^-$ as well as for a $BABCO^-$ surrounded by the five BABCO units which in the crystal act as hydrogen bond acceptors from the three $-CH_2-CH_2-$ groups of the rotor with C_{sp3}–H···O contacts shorter than 2.90 Å. Since the only important bonding interactions are the hydrogen bonds, to simulate the five units of the rotor environment, instead of the full rotors, we used CH_3—C≡C—COOH and/or CH_3—C≡C—COO^- exactly in the same position as in the crystal

dx.doi.org/10.1021/ja301484b | J. Am. Chem. Soc. 2012, 134, 7880–7891

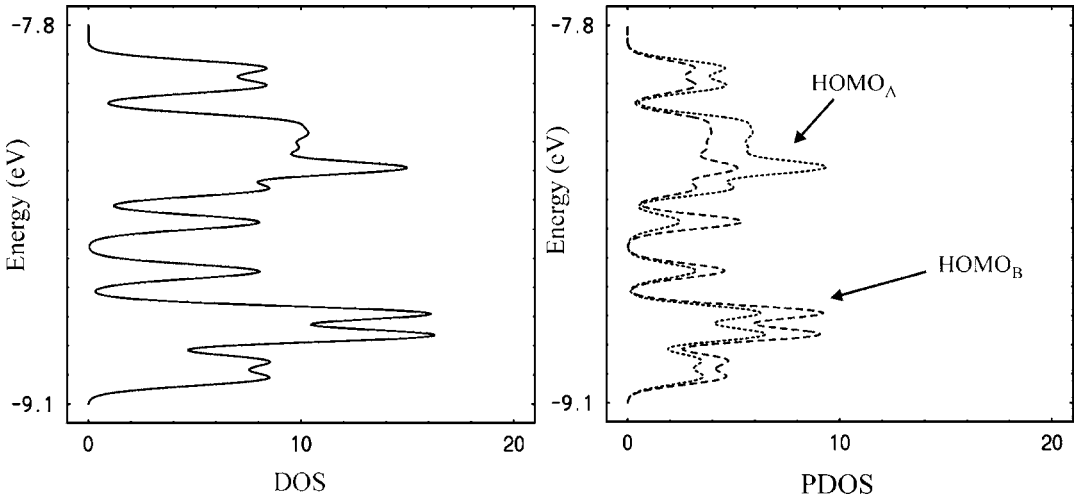

Figure 10. (a) Calculated density of states (in units of electrons/eV unit cell] in the region of the HOMO bands. (b) Projected density of states (PDOS) of the HOMO of the A donors (···) and the B donors (---) for the donor layers of $(EDT\text{-}TTF\text{-}CONH_2)_2^+[BABCO^-]$.

structure. This allows a considerable saving of computer time and better quality calculations. For the rotor we used a slightly symmetrized version of the unit in the crystal structure; namely, the terminal −COOH and $-COO^-$ groups were placed in the plane of one of the three components of the rotor, as shown in Figure 11.

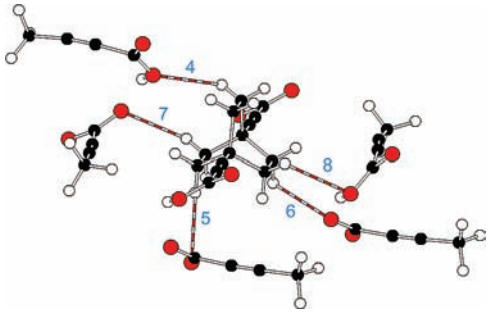

Figure 11. Discrete $BABCO^-$ surrounded by the five $CH_3—C\equiv C—COOH$ and/or $CH_3—C\equiv C—COO^-$ units used in the calculations as a model of its H-bonded environment.

Calculations were carried out using two different functionals: B3LYP[22] and M06-2X[23] (which usually describe slightly better the hydrogen bonds). As a test for the quality of the calculations we first computed the rotational barrier for ethane and found 2.70 and 2.74 kcal mol^{-1} with the B3LYP and M06-2X functionals, respectively. These values are in excellent agreement with the experimental value of 2.90 kcal mol^{-1}.[32] We calculated the rotational barrier in three different ways: (i) for the free $BABCO^-$; (ii) for $BABCO^-$ in the presence of three $CH_3—C\equiv C—COO^-$ and two $CH_3—C\equiv C—COOH$ exactly as in the solid and without any structural optimization; and (iii) for $BABCO^-$ in the presence of three $CH_3—C\equiv C—COO^-$ and two $CH_3–C\equiv C—COOH$ as in the solid with the additional feature that the six $-CH_2$ groups of the rotor were optimized for every value of the rotational angle θ. The results obtained with the two functionals are very similar (for instance calculation ii led to a barrier of 6.3 kcal mol^{-1} with M06-2X and 7.4 kcal mol^{-1} with B3LYP).

The M06-2X calculated rotational barrier for the free $BABCO^-$ is quite small, 0.1 kcal mol^{-1}, indicating that the rotation is essentially barrierless in the absence of intermolecular interactions. The rotational barrier calculated with the effect of the set of hydrogen bonds defining the rotors environment amounts to 7.3 kcal mol^{-1}; the energetic profile is shown in Figure 12. Increasing the basis set so as to include

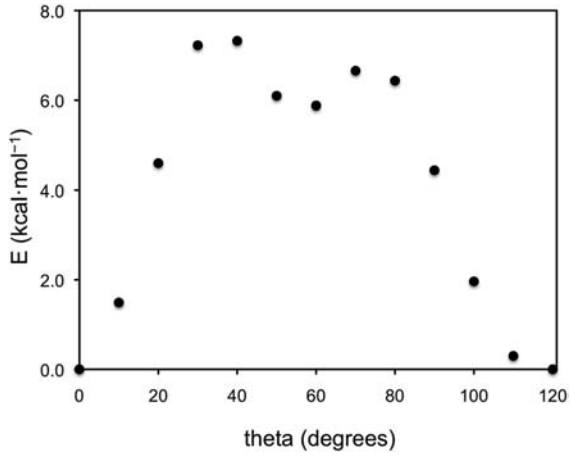

Figure 12. M06-2X calculated rotational barrier for $BABCO^-$ in the solid (modeled as in Figure 11) with the two carbonyl groups placed in the same plane which consequently is also the plane of one of the three blades of the rotor, a configuration which defines the angle zero of the plot. This structure is a minimum because the stabilization provided by the hydrogen bonds in the crystal is optimized. Rotation leads to the progressive loss of this stabilization and thus the energy goes up.

diffuse functions for all atoms including hydrogen (M06-2X/6-311++G(d,p) calculations) has a minor effect on the rotational profile (the calculated rotational barrier is 7.0 kcal mol^{-1}). Therefore, we conclude that the coupling induced by the cooperativity between those five C_{sp3}–H···O hydrogen bonds has a strong effect on the rotational barrier and most likely contributes to impede the rotational motion in $(EDT\text{-}TTF\text{-}CONH_2)^+_2[BABCO^-]$.

Motion of BCO Rotors Might Become Dissipative in a Highly Conducting Solid. Colorless $[n Bu_4N^+]_2[BABCO]\text{-}[BABCO^-]_2$ is a large band gap insulator, and there is no free carrier available. Because the rotational barrier observed for

dx.doi.org/10.1021/ja301484b | J. Am. Chem. Soc. 2012, 134, 7880−7891

$(EDT\text{-}TTF\text{-}CONH_2)_2^+[BABCO^-]$ is so large, one is compelled to assess this question from the viewpoint of the difference in the electrical properties of the two compounds rather than to the sole effect of intermolecular interactions in the ground state. Hence, we now comment on another, complementary channel by which the BCO rotators might be slowed down to a significant extent in highly conducting crystals of $(EDT\text{-}TTF\text{-}CONH_2)_2^+[BABCO^-]$.

One especially fascinating problem in quantum physics is to consider a quantum system coupled to a macroscopic bath. In that case novel physics is expected to occur since the presence of the bath can lead to the suppression of tunneling.[33] This is known to lead to quantum phase transitions driven by dissipation.[34] This class of problems has been intensively studied, and dissipative quantum systems have been realized in systems such as noisy Josephson junctions or quantum wires.[35] From that viewpoint, in $(EDT\text{-}TTF\text{-}CONH_2)_2^+[BABCO^-]$, an unprecedented example where a molecular rotor is a constituent of a molecular metal, the quantum physics[36] inherent to its low dimensional electronic and crystal structures provides a dissipation channel for the energy associated with the rotor dynamics. In any insulating crystalline solid investigated to date, like BIBCO and, here, $[n\text{Bu}_4N^+]_2[BABCO][BABCO^-]_2$, the rotational movement of the BCO fragment is typically frictionless. In a highly conducting crystal of $(EDT\text{-}TTF\text{-}CONH_2)_2^+[BABCO^-]$, two systems interact, namely, the quantum system of mobile carriers within $EDT\text{-}TTF\text{-}CONH_2$ slabs, and two rotational degrees of freedom: the rotation around the rotor axle, which may be either classical, or quantum even on account of the barrier for the isolated rotor calculated to be as low as 0.1 kcal mol^{-1}; and the torsion around the axles of each rotor blade which interconvert and change the rotor chirality by quantum tunneling, as recently reported[37] in the analogous 1,4-diazabicyclo[2.2.2]octane (DABCO). In such a case, the large number of degrees of freedom[36,38] of the low dimensional electron gas serves as a bath for the dissipation of the energy of moving rotors provided that a coupling exists between the two systems. This coupling is simply due to the Coulomb interaction between the charges of the rotors and the charges of the carriers. The movement of the electrons in the conducting slabs produces transient currents and, therefore, dissipation since the resistivity has a finite value. Hence, there is a net transformation of the energy of the rotors' motion into heat as a result of the Joule effect in the conducting layers. However, even in the case of quantum dissipation, the temperature dependence of the rotation frequency can still be described in the simplest approximation by an Arrhenius law.[33] However, it can be expected to have an impact on the prefactor. At the theoretical level, the full study of the interplay between the two phenomena requires addittional calculations beyond the present scope of this paper. On the experimental side, an interesting goal would now be to prepare a metallic salt with a rotor where the hydrogen bond friction inherent to the C−H donors of the rotor blades would have vanished for the most part so that the actual contribution of quantum dissipation to the damping of the rotors could be tested further.

It is of interest to note that the fluidity of the rotors' motion should be recovered in the insulating ground state below 50 K (Figure 6b). Unfortunately, at this temperature the rotors are typically frozen as shown in Figure 2 for the insulator $[n\text{Bu}_4N^+]_2[BABCO][BABCO^-]_2$.

CONCLUSION

Our idea that combining recent concepts from the fields of molecular conductivity and molecular machinery to design a crystalline molecular conductor that also possesses a molecular rotor where the coupling of the two systems may produce interesting new phenomena is illustrated by the study of the structures, electronic and physical properties, and dynamics of two solids with a common 1,4-bis(carboxyethynyl)-bicyclo[2.2.2]octane (BABCO) functional rotor: $[n\text{Bu}_4N^+]_2[BABCO][BABCO^-]_2$ is a colorless insulator where the dicarboxylic acid cocrystallizes with two of its monoanionic conjugated base; in the other, $(EDT\text{-}TTF\text{-}CONH_2)_2^+[BABCO^-]$, highly conducting molecular slabs and anionic rotors are assembled, intertwined in black, shiny crystalline needles. Using variable-temperature proton spin−lattice relaxation, $^1H\ T_1^{-1}$, the Brownian rotators which move at 120 GHz at 300 K in $[n\text{Bu}_4N^+]_2[BABCO][BABCO^-]_2$ are unambiguously assigned to the BABCO sites with a rotational barrier of 2.03 kcal mol^{-1} (1020 K), while the rotors on the $BABCO^-$ sites experience stochastic 32 GHz jumps at 300 K over a rotational barrier of 2.72 kcal mol^{-1} (1370 K). In contrast, the $BABCO^-$ rotors are essentially braked in within the highly conducting crystals of $(EDT\text{-}TTF\text{-}CONH_2)_2^+[BABCO^-]$, whose room temperature conductivity, 5 S cm^{-1} at 1 bar, increases rapidly with pressure up to 50 S cm^{-1} at 11.5 kbar. The calculated band structure and Fermi surface qualify as a quasi-ideal 2D metal although the crystal structure analysis suggests a charge-ordered insulator. Two regimes with different activation energies E_a for the resistivity (180 K above 50 and 400 K below) are observed at ambient pressure; a metallic state is stabilized at ca. 8 kbar, and an insulating ground state remains below 50 K at all pressures.

The discovery of such contrasted dynamics of the Brownian rotators in $[n\text{Bu}_4N^+]_2[BABCO][BABCO^-]_2$ and $(EDT\text{-}TTF\text{-}CONH_2)_2^+[BABCO^-]$ prompted us to identify and asses two likely channels by which the motion of the rotors might become damped in the highly conducting solid. The first one is defined as a low-velocity viscous regime induced by the cooperativity between five C_{sp3}−H···O hydrogen bonds between a rotor and five BABCO units in its environment, a situation unique to the structure of this molecular conductor as it emerged from the analysis of the contrasted environments of the rotors within the structures of the two solids. The rotational barrier calculated with the effect of this set of hydrogen bonds defining the rotors environment amounts to 7.3 kcal mol^{-1}. Therefore, we conclude that hydrogen bond interactions have a strong effect on the rotational barrier and most likely contribute to the damping of the rotational motion in $(EDT\text{-}TTF\text{-}CONH_2)_2^+[BABCO^-]$.

A complementary approach of the difference of dynamics of the rotors in the two solids is proposed from the viewpoint of the difference in the electrical properties of **2** and **3**, rather than to the sole effect of intermolecular interactions in the ground state. Hence, we have discussed the possibility that, in a highly conducting crystal of $(EDT\text{-}TTF\text{-}CONH_2)_2^+[BABCO^-]$, the large number of degrees of freedom of the low dimensional electron gas may serve as a bath for the dissipation of the energy of moving rotors, the two systems being coupled by the Coulomb interaction between the charges of the rotors and the charges of the carriers. The movement of the electrons in the conducting slabs produces transient currents and, therefore, dissipation since the resistivity has a finite value. Hence, there is

dx.doi.org/10.1021/ja301484b | J. Am. Chem. Soc. 2012, 134, 7880−7891

a net transformation of the energy of the rotors' motion into heat as a result of the Joule effect in the conducting layers.

A major outcome of the present study is the revelation that hydrogen bond interactions and quantum dissipation stand out as two defining, fascinating problems in the chemistry, physical chemistry, and physics of conducting crystalline molecular machines; here, two dynamics are entangled, that of low dimensional electrons and that of the rotators' molecular degrees of freedom. The results disclosed in the present work offer the opportunity to explore further the interplay between fluctuations and dissipation phenomena in *molecular* systems, an exciting, new direction in chemistry in a context of current intensive research in condensed matter physics.

■ ASSOCIATED CONTENT

Supporting Information

Additional crystallographic information and Cartesian coordinates for the partially optimized structures of Scheme 3 for rotational angles $\theta = 0°$ and 40°. This material is available free of charge via the Internet at http://pubs.acs.org.

■ AUTHOR INFORMATION

Corresponding Author

patrick.batail@univ-angers.fr; canadell@icmab.es; pawel.wzietek@u-psud.fr; Thierry.Giamarchi@unige.ch; mgg@chem.ucla.edu

Notes

The authors declare no competing financial interest.

■ ACKNOWLEDGMENTS

This work was supported by the Interdisciplinary ANR Project 3/4-Filled 2009-2011 (ANR-08-BLAN-0140-01) and the Région des Pays de la Loire Grant MOVAMOL-2010 10306. We thank the CNRS for a Ph.D. grant to C.L., the Spanish Ministerio de Educación y Ciencia (Projects FIS2009-1271-C04-03, CTQ2011-29054-C02-01, and CSD 2007-00041). Work at UCLA was supported by NSF Grant DMR1101934. Work at the University of Geneva was supported in part by the Swiss SNF under MaNEP and Division II.

■ REFERENCES

(1) Horinek, D.; Michl, J. *Proc. Natl. Acad. Sci. U.S.A.* **2005**, *102*, 14175.

(2) (a) Akutagawa, T.; Nakamura, T. *Dalton Trans.* **2008**, 6335. (b) Akutagawa, T.; Shitagami, K.; Nishihara, S.; Takeda, S.; Hasegawa, T.; Nakamura, T.; Hosokoshi, Y.; Inoue, K.; Ikeuchi, S.; Miyazaki, Y.; Saito, K. *J. Am. Chem. Soc.* **2005**, *127*, 4397. (c) Akutagawa, T.; Koshinaka, H.; Sato, D.; Takeda, S.; Noro, S.-I.; Takahashi, H.; Kumai, R.; Tokura, Y.; Nakamura, T. *Nat. Mater.* **2009**, *8*, 342.

(3) (a) El-Ghayoury, A.; Mézière, C.; Simonov, S.; Zorina, L.; Cobián, M.; Canadell, E.; Rovira, C.; Náfrádi, B.; Sipos, B.; Forró, L.; Batail, P. *Chem.—Eur. J.* **2010**, *16*, 14051. (b) Lakhdar, Y.; Mézière, C.; Zorina, L.; Giffard, M.; Batail, P.; Canadell, E.; Auban-Senzier, P.; Pasquier, C.; Jérome, D.; Náfrádi, B.; Fórró, L. *J. Mater. Chem.* **2011**, *21*, 1516.

(4) It has been shown that the dielectric modulation inherent to hydrogen bonding and bromide anions dynamics is coupled to Mott localization at a metal-to-insulator transition that sets upon charge ordering and Wigner crystallization in $(EDT\text{-}TTF\text{-}CONMe_2)_2Br$: Zorina, L.; Simonov, S.; Mézière, C.; Canadell, E.; Suh, S.; Brown, S. E.; Foury-Leylekian, P.; Fertey, P.; Pouget, J.-P.; Batail, P. *J. Mater. Chem.* **2009**, *19*, 6980.

(5) Giamarchi, T. *Chem. Rev.* **2004**, *104*, 5037.

(6) Seo, H.; Hotta, C.; Fukuyama, H. *Chem. Rev.* **2004**, *104*, 5005.

(7) Miyagawa, K.; Kanoda, K.; Kawamoto, A. *Chem. Rev.* **2004**, *104*, 5635.

(8) (a) Scarso, A.; Onagi, H.; Rebek, J., Jr. *J. Am. Chem. Soc.* **2004**, *126*, 12728. (b) Kottas, G. S.; Clarke, L. I.; Horinek, D.; Michl, J. *Chem. Rev.* **2005**, *105*, 1281. (c) Browne, W. R.; Feringa, B. L. *Nat. Nanotechnol.* **2006**, *1*, 25. (d) Kay, E. R.; Leigh, D. A.; Zerbetto, F. *Angew. Chem., Int. Ed.* **2007**, *46*, 72. (e) Skopek, K.; Hershberger, M. C.; Gladysz, J. A. *Coord. Chem. Rev.* **2007**, *251*, 1723. (f) Michl, J.; Charles, E.; Sykes, H. *ACS Nano* **2009**, *3*, 1042. (g) Skopek, K.; Gladysz, J. A. *J. Organomet. Chem.* **2008**, *693*, 857. (h) Karim, A. R.; Linden, A.; Baldridge, K. K; Siegel, J. S. *Chem. Sci.* **2010**, *1*, 102.

(9) For the definition of amphidynamic crystals and leading references, see: Karlen, S. D.; Reyes, H.; Taylor, R. E.; Khan, S. I.; Hawthorne, M. F.; Garcia-Garibay, M. A. *Proc. Natl. Acad. Sci. U.S.A.* **2010**, *107*, 14973.

(10) (a) Kathirgamanathan, P.; Mucklejohn, S. A.; Rosseinsky, D. R. *J. Chem. Soc., Chem. Commun.* **1979**, 86−87. (b) Giffard, M.; Riou, A.; Mabon, G.; Mercier, N.; Molinié, P.; Phap Nguyen, T. *J. Mater. Chem.* **1999**, *9*, 851. (c) Mercier, N.; Giffard, M.; Pilet, G.; Allain, M.; Hudhomme, P.; Mabon, G.; Levillain, E.; Gorgues, A.; Riou, A. *J. Chem. Soc., Chem. Commun.* **2001**, 2722. (d) Geiser, U.; Schlueter, J. A. *Chem. Rev.* **2004**, *104*, 5203. (e) Lakhdar, Y.; El-Ghayoury, A.; Zorina, L.; Mercier, N.; Allain, M.; Mézière, C.; Auban-Senzier, P.; Batail, P.; Giffard, M. *Eur. J. Inorg. Chem.* **2010**, 3338.

(11) (a) Armand, M.; Grugeon, S.; Vezin, H.; Laruelle, S.; Ribiere, P.; Poizot, P.; Tarascon, J.-M. *Nat. Mater.* **2009**, *8*, 120. (b) Walker, W.; Grugeon, S.; Vezin, H.; Laruelle, S.; Armand, M.; Tarascon, J.-M.; Wudl, F. *J. Am. Chem. Soc.* **2010**, *132*, 6517. (c) Walker, W.; Grugeon, S.; Vezin, H.; Laruelle, S.; Armand, M.; Wudl, F.; Tarascon, J.-M. *J. Mater. Chem.* **2011**, *21*, 1615.

(12) (a) Baudron, S. A.; Batail, P.; Rovira, C.; Canadell, E.; Clérac, R. *Chem. Commun.* **2003**, 1820. (b) Heuzé, K.; Mézière, M.; Fourmigué, M.; Batail, P.; Coulon, C.; Canadell, E.; Auban-Senzier, P.; Jérome, D. *Chem. Mater.* **2000**, *12*, 1898. (c) Fourmigué, M.; Batail, P. *Chem. Rev.* **2004**, *104*, 5379. (d) Baudron, S. A.; Batail, P.; Coulon, C.; Clérac, R.; Canadell, E.; Laukhin, V.; Melzi, R.; Wzietek, P.; Jérome, D.; Auban-Senzier, P.; Ravy, S. *J. Am. Chem. Soc.* **2005**, *127*, 11785.

(13) (a) Lemouchi, C.; Vogelsberg, C.; Simonov, S.; Zorina, L.; Batail, P.; Brown, S.; Garcia-Garibay, M. A. *J. Am. Chem. Soc.* **2011**, *133*, 6371. (b) Lemouchi, C.; Vogelsberg, C.; Simonov, S.; Zorina, L.; Batail, P.; Brown, S.; Garcia-Garibay, M. A. *J. Am. Chem. Soc.* **2011**, *133*, 13765 (Addition/Correction).

(14) Saravanakumar, R.; Varghese, B.; Sankararaman, S. *CrystEngComm* **2009**, *11*, 337.

(15) Batail, P.; Boubekeur, K.; Fourmigué, M.; Gabriel, J. C. P. *Chem. Mater.* **1998**, *10*, 3005.

(16) Heuzé, K.; Fourmigué, M.; Batail, P. *J. Mater. Chem.* **1999**, *9*, 2373.

(17) Sheldrick. G. M. *SADABS—Bruker Nonius Area Detector Scaling and Absorption Correction-V2.10*; 2003.

(18) Sheldrick, G. M. *Acta Crystallogr.* **2008**, *A64*, 112.

(19) Whangbo, M.-H.; Hoffmann, R. *J. Am. Chem. Soc.* **1978**, *100*, 6093.

(20) Ammeter, J. H.; Bürgi, H.-B.; Thibeault, J.; Hoffmann, R. *J. Am. Chem. Soc.* **1978**, *100*, 3686.

(21) (a) Pénicaud, A.; Boubekeur, K.; Batail, P.; Canadell, E.; Auban-Senzier, P.; Jérome, D. *J. Am. Chem. Soc.* **1993**, *115*, 4101. (b) Baudron, S. A.; Avarvari, N.; Canadell, E.; Auban-Senzier, P.; Batail, P. *Chem.—Eur. J.* **2004**, *10*, 4498.

(22) Becke, A. D. *J. Chem. Phys.* **1993**, *98*, 5648.

(23) Zhao, Y.; Truhlar, D. G. *Theor. Chem. Acc.* **2008**, *120*, 215−241.

(24) Frisch, M. J.; Trucks, G. W.; Schlegel, H. B.; Scuseria, G. E.; Robb, M. A.; Cheeseman, J. R.; Scalmani, G.; Barone, V.; Mennucci, B.; Petersson, G. A.; Nakatsuji, H.; Caricato, M.; Li, X.; Hratchian, H. P.; Izmaylov, A. F.; Bloino, J.; Zheng, G.; Sonnenberg, J. L.; Hada, M.; Ehara, M.; Toyota, K.; Fukuda, R.; Hasegawa, J.; Ishida, M.; Nakajima, T.; Honda, Y.; Kitao, O.; Nakai, H.; Vreven, T.; Montgomery, J. A., Jr.; Peralta, J. E.; Ogliaro, F.; Bearpark, M.; Heyd, J. J.; Brothers, E.; Kudin, K. N.; Staroverov, V. N.; Kobayashi, R.; Normand, J.; Raghavachari, K.;

Rendell, A.; Burant, J. C.; Iyengar, S. S.; Tomasi, J.; Cossi, M.; Rega, N.; Millam, J. M.; Klene, M.; Knox, J. E.; Cross, J. B.; Bakken, V.; Adamo, C.; Jaramillo, J.; Gomperts, R.; Stratmann, R. E.; Yazyev, O.; Austin, A. J.; Cammi, R.; Pomelli, C.; Ochterski, J. W.; Martin, R. L.; Morokuma, K.; Zakrzewski, V. G.; Voth, G. A.; Salvador, P.; Dannenberg, J. J.; Dapprich, S.; Daniels, A. D.; Farkas, Ö.; Foresman, J. B.; Ortiz, J. V.; Cioslowski, J.; Fox, D. J. *Gaussian 09, revision A.02*; Gaussian, Inc.: Wallingford, CT, 2009.

(25) Krishnan, R.; Binkley, J. S.; Seeger, R.; Pople, J. A. *J. Chem. Phys.* **1980**, *72*, 650.

(26) Ranganathan, A.; El-Ghayoury, A.; Zorina, L.; Batail, P. *CrystEngComm* **2010**, *12*, 4268.

(27) Note that molecular dynamics calculation have given access to similar activation energies for other compounds, see: Akimov, A. V.; Kolomeisky, A. B. *J. Phys. Chem. C* **2011**, *115*, 13584.

(28) Echeverría, J.; Aullon, G.; Danovich, D.; Shaik, S.; Alvarez, S. *Nat. Chem.* **2011**, *3*, 323.

(29) Whangbo, M.-H.; Williams, J. M.; Leung, P. C. W.; Beno, M. A.; Emge, T. J.; Wang, H. H. *Inorg. Chem.* **1985**, *24*, 3500.

(30) For instance, although they are not strictly comparable because the donor is not exactly the same, the total dispersion here is 37% larger than in the localized (EDT-TTF-CONMe$_2$)AsF$_6$ salt at room temperature: Heuzé, K.; Fourmigué, M.; Batail, P.; Coulon, C.; Clérac, R.; Canadell, E.; Auban-Senzier, P.; Ravy, S.; D. Jérome, D. *Adv. Mater.* **2003**, *15*, 1251 and ref 4.

(31) Mori, T. *Bull. Chem. Soc. Jpn.* **1999**, *72*, 2011.

(32) Pitzer, R. M. *Acc. Chem. Res.* **1983**, *16*, 207.

(33) Caldeira, A. O.; Leggett, A. J. *Ann. Phys. (N.Y.)* **1983**, *149*, 374.

(34) (a) Bray, A. J.; Moore, M. A. *Phys. Rev. Lett.* **1982**, *49*, 1545. (b) Chakravarty, S. *Phys. Rev. Lett.* **1982**, *49*, 681.

(35) (a) Caldeira, A.; Leggett, A. J. *Phys. Rev. Lett.* **1981**, *46*, 211. (b) Leggett, A. J.; Chakravarty, S.; Dorsey, A. T.; Fisher, M. P. A; Garg, A.; Zwerger, W. *Rev. Mod. Phys.* **1987**, *59*, 1.

(36) See ref 5 and Giamarchi, T. *Quantum Physics in One Dimension*; Clarendon Press: Oxford, 2004.

(37) Gabuda, S. P.; Kozlova, S. G.; Samsonenko, D. G.; Dybtsev, D. N.; Fedin, V. P. *J. Phys. Chem. C* **2011**, *115*, 20460.

(38) See: Lobos, A. M.; Iucci, A.; Müller, M.; Giamarchi, T. *Phys. Rev. B* **2009**, *80*, 214515 and references therein.